Supporting Information:

Inelastic Surface Scattering of Vibrationally Excited N_2: Role of Multi-Quantum De-Excitations

Floris van den Bosch*

Nick Gerrits

Jörg Meyer†

Leiden Institute of Chemistry, Gorlaeus Laboratories,

Leiden University, P.O. Box 9502, 2300 RA Leiden, The Netherlands

*f.van.den.bosch@lic.leidenuniv.nl

†j.meyer@chem.leidenuniv.nl

Contents

S1 Additional Computational Details

S1.1 Density Function Theory Calculations

The DFT calculations for the training of the HDNNP were performed by Shakouri et al. [1], which we will briefly summarize here: Version 5.3.5 of VASP was used with a plane wave kinetic energy of 550 eV. The Brillouin zone was sampled using a Γ-centered 7×7×1 k-point grid employing Methfessel-Paxton smearing with a width of 0.3 eV. The pseudopotentials used were the VASP PAW pseudopotentials: **Ru_pv** with a Zn core for ruthenium, and **N** with a He core for nitrogen.

S1.2 Neural Network Potential

In Fig. S1, we present two potential energy surface (PES) cuts, yielded by the high-dimensional neural network potential [1]. Fig. S1a displays the potential energy of a N_2 molecule with varying bond length. Here we compare the HDNNP to a Morse potential with parameters derived from vibrational constants [2] and with equilibrium bond length equal to the HDNNP. We see that for the vibrational states up to $\nu = 8$, i.e., $E_{\text{vib}} = 2.387$ eV, these two potentials are nearly identical. The dissociation energy of the Morse potential is in better agreement with the dissociation energy of ∼10 eV [2]. We show the curves up to a bond length of 2.65 Å, which is the criterion for dissociation in our molecular dynamics run and thus the upper limit of the bond length in these simulations. Fig. S1b shows a cut through the PES for $u = v = 0.504$ and the orientation of the molecule is given by $\phi = 30°, \theta = 84.3°$. This cut goes through the minimum transition state with a barrier height of 1.84 eV.

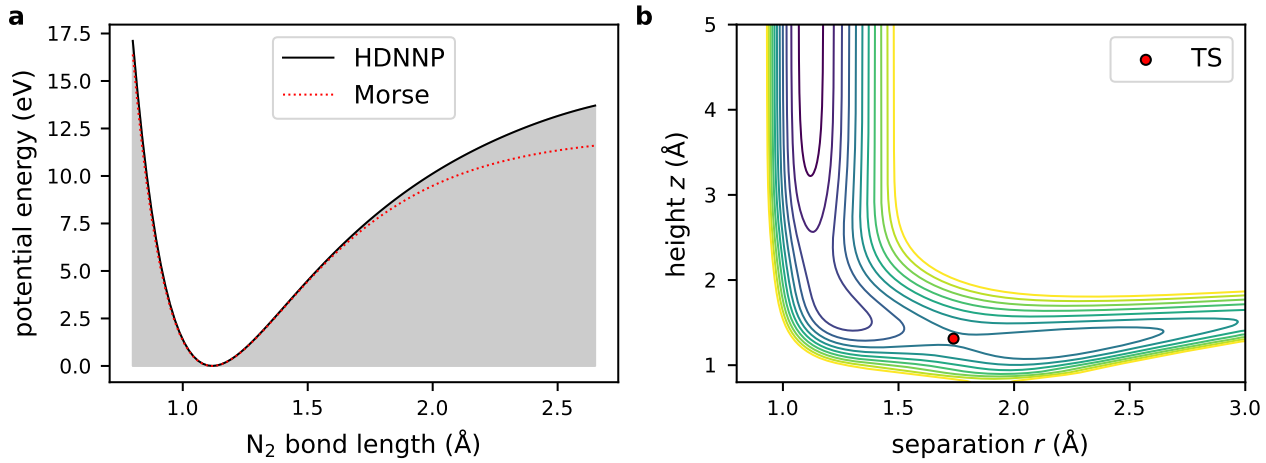

Figure S1: (a) Potential energy as function of the N_2 bond length computed with the HDNNP (black line) compared to a Morse potential (red dotted line). (b) Potential energy surface as function of bond length (r) and the height (z) of the N_2 center of mass above the Ru(0001) surface. Transition state is indicated in red.

S1.3 Quasi-Classical Sampling of Initial Vibrational States

As detailed in Section 2.1, the initial vibrational energy is determined by the energy eigenvalues of the Schrödinger equation for the molecular vibration. However, the initial condition of the vibration (i.e. bond length and velocity) is not sampling according to the wavefunction, but instead sampled from a short classical trajectory of the vibration. Fig. S2 depicts the difference in distributions of the initial bond length both as dictated by the wave function (a) and by a uniform sampling of the phase of the vibration of a classical trajectory. In the quantum case (Fig. S2a), the distribution is smooth with a number of nodes equal to the vibrational quantum number ν. It is very close to the solutions of the harmonic oscillator. The classical distribution (Fig. S2b) shows no nodes and is not continuous at the classical turning points. There, the probability density reaches maxima as the vibration is the slowest and thus spends more time there. As the vibrational quantum number increases, the correspondence between the quantum and classical distributions becomes higher as the wave function becomes more weighted towards the classical turning point.

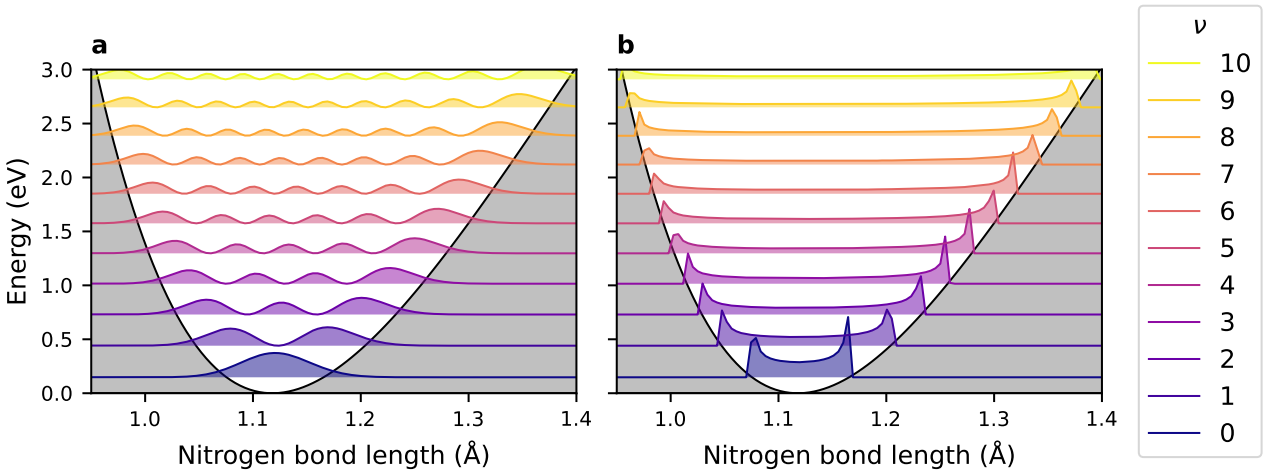

Figure S2: Energy and distribtions of the N_2 bond length according to the nuclear wave fucntion (a) and classical trajectories of the vibration at the same energy eigenvalues (b). The latter is used to sample the initial conditions in the quasi-classical trajectory method Section 2.1

S2 Further Analysis of Scattering Angle Distributions

S2.1 Scattering Angle Binning

To mimic the experimental measurements as closely as possible, the results from Fig. 2 are obtained by binning the scattering directions over spherical caps centered at the outgoing polar angle θ_{out} and azimuthal deviation from the scattering plane of $\Delta\phi = 0$. The angle radius of this spherical cap was taken to be 2.5°. The bins and center points are depicted in Fig. S3. The bin count is computed by determining the angle between the bin center and the

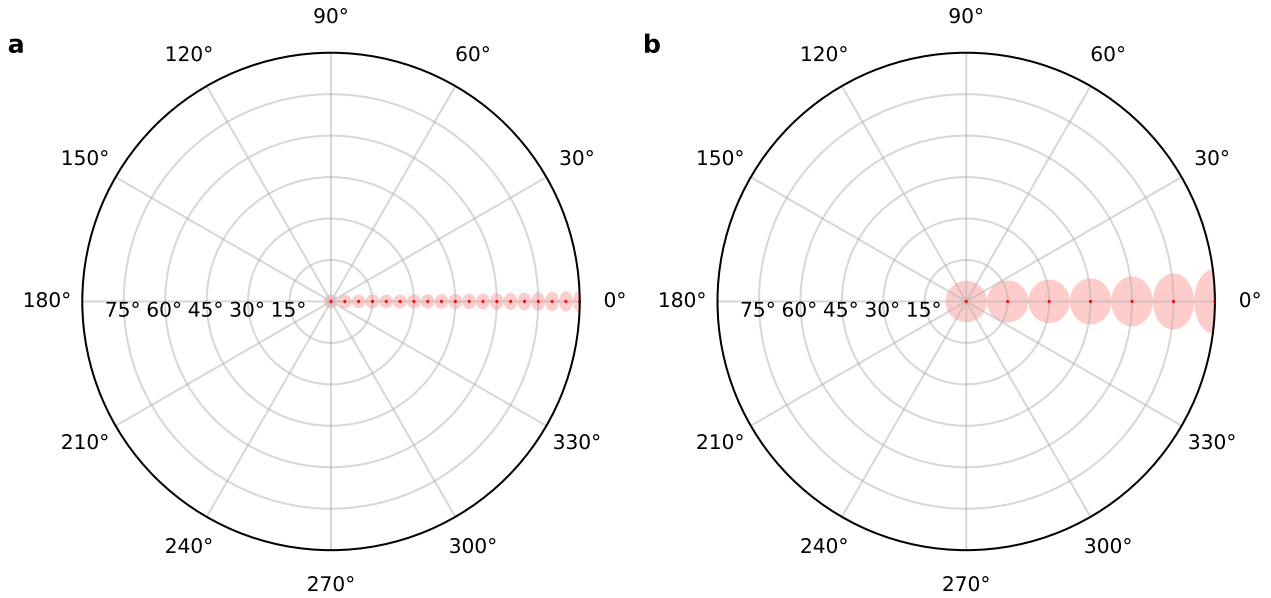

Figure S3: Illustration of the spherical binning of scattering angles. (a) Bins with angle radius of 2.5° as used for Fig. 2. (b) Larger Bins with angle radius of 7.5° for increased visibility of the bins size and shapes. The radial axis denote the polar scattering angle and the angular axis denotes the azimuthal scattering angle. Note that in reality the bins are perfectly symmetric spherical caps and are only distorted due to the projection.

scattering vector using

$$\alpha = \cos^{-1}\left(\sin\theta_1 \sin\theta_2 \cos\Delta\phi + \cos\theta_1 \cos\theta_2\right), \tag{S1}$$

which is the angular distance of two points on the sphere.

With this method, we determine the scattering distributions of the entire hemisphere as shown in Fig. S4. Here, we see that the spread of the scattering distribution in the azimuthal direction is of similar magnitude as the spread in the polar angle. Furthermore, we see that for the simulations at $\theta_{\text{inc}} = 60°$ the scattering is much more specular than at 40°. Comparing the ground-state and plasma distributed beams, we see that for the plasma beam the amount

of far outliers from the specular peak is increased and the sharpness of the specular peak is decreased.

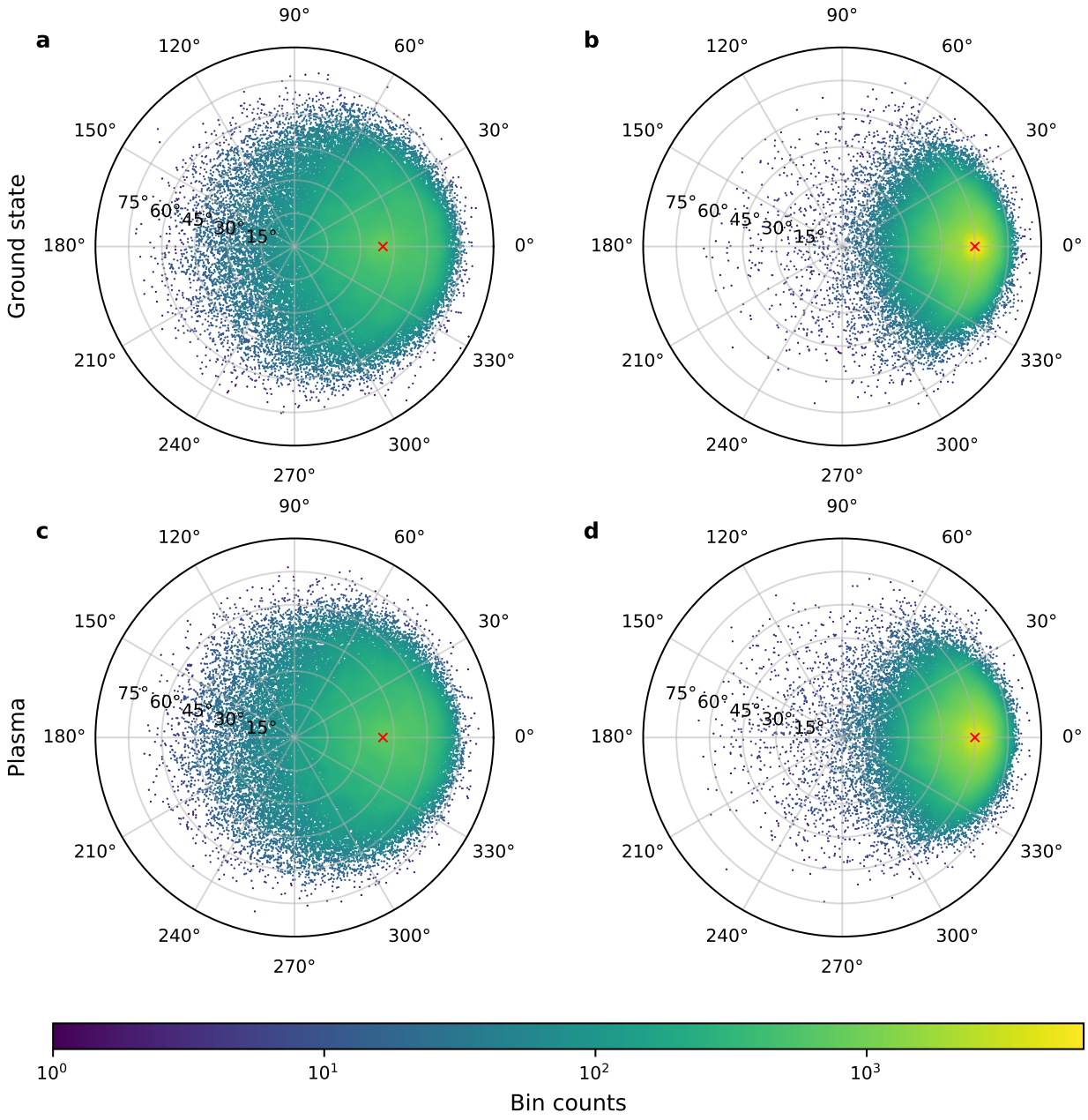

Figure S4: Distribution of scattering angles in terms of outgoing polar angle θ_{out} (radial axis) and angle deflection from the incident plane $\Delta\phi$ (angular axis). Distributions are calculated for incident polar angles of 40° (a, c) and 60° (b, d) for N_2 molecules in the ground state (a, b) and like a rovibrationally hot plasma with $T_{\text{vib}} = T_{\text{rot}} = 2000\,\text{K}$ (c, d). The color of each point corresponds to number of points within a 2.5° spherical cap bin as described in Section S2.1. The red crosses indicate the ideal specular reflection direction.

S2.2 Surface Orientation Dependence

In our simulations of the experiments by Zaharia et al. [3], we randomly sample the azimuthal orientation of N_2 with respect to the Ru(0001) surface. However, this may not accurately represent the experiments, since it is possible that this orientation was experimentally fixed. To investigate the errors this approximation may introduce, we investigate the scattering angle quasi-classical trajectory (QCT) results of normally incident monochromatic beams.

In Fig. S5, we show the scattering angle distribution on the full hemisphere at low and high incidence energy. At low incidence energy (0.5 eV), the scattering angle is only minimally dependent on the direction of the lattice. At high incidence energies (4.25 eV), which are more representative for the experiments, we do see an orientation dependence of the scattering: Along lattice vectors the polar angle distribution's peak is broader than halfway between lattice vectors, but the range of the distribution is smaller.

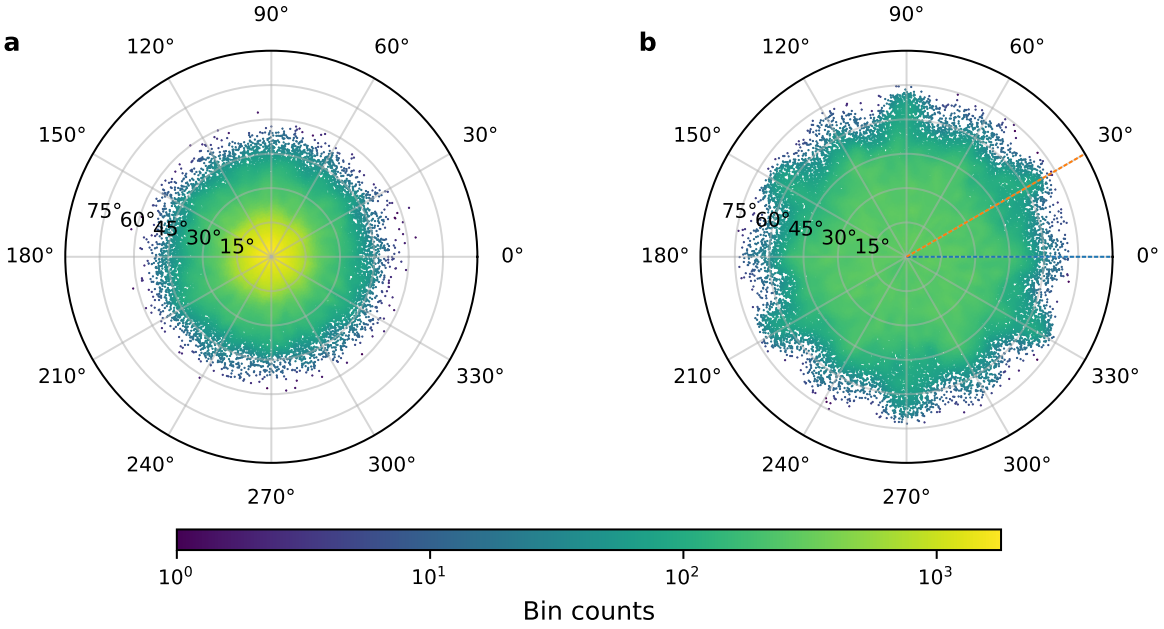

Figure S5: Distribution of scattering angles in terms of outgoing polar angle θ_{out} (radial axis) and azimuthal angle ϕ_{out} from the first unit cell vector (angular axis). For these trajectories, the incident velocity of the N_2 molecule was taken normal to the surface with incidence energy of 0.5 eV (a) and 4.25 eV (b) with the molecule in the vibrational ground state. The color of each point corresponds to number of points within a 2.5° spherical cap bin as described in Section S2.1. The blue and orange dashed lines in (b) indicate slices of the distribution along $\phi_{\text{out}} = 0°$ and 30°. The corresponding polar angle distributions are shown in Fig. S6.

The magnitude of this effect can be seen in Fig. S6, where we have taken slices through the distribution at $\phi_{\text{out}} = 0°$ (aligned with lattice vector) and $\phi_{\text{out}} = 30°$ (halfway between lattice vectors). The large differences between these two slices illustrate that the polar angular distribution depends on the alignment of the surface with the molecular beam. This implies

that the distributions of Fig. 2 might be systematically different from our results due to the alignment of the surface sample.

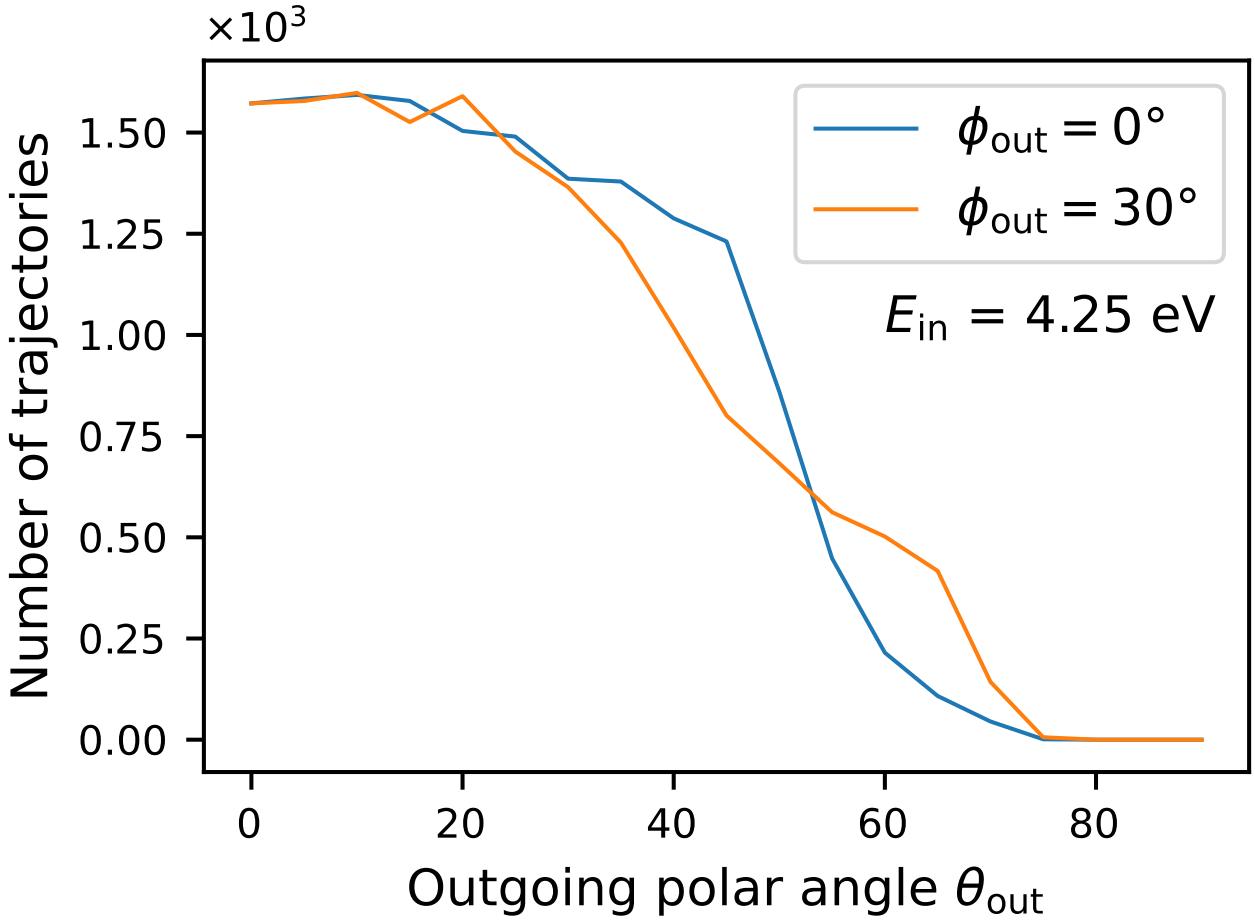

Figure S6: Distribution of scattered polar angles θ_{out} at outgoing azimuthal angles ϕ_{out} of 0° (blue) and 30° (orange) w.r.t the first unit cell vector. The vertical axis displays number of trajectories scattered within a 2.5° spherical cap bin as described in Section S2.1. Equivalent slices through the full hemispherical scattering distribution are indicated in Fig. S5

In Fig. S7, we present the direction of scattered N_2 molecules dependent on the impact site in the surface unit cell. In the low-energy regime (0.5 eV), the scattering direction smoothly changes with the impact site above a single surface atom (white circle in Fig. S7). This suggests that only one surface atom significantly interacts with the molecule. At higher incidence energies (4.25 eV), this is not the case as there are much more sudden jumps in direction across the crystallographic directions, while being relatively constant between them. Here, the molecule seems to scatter from facets in the surface instead of single atoms. This in turn results in surface orientation dependent scattering.

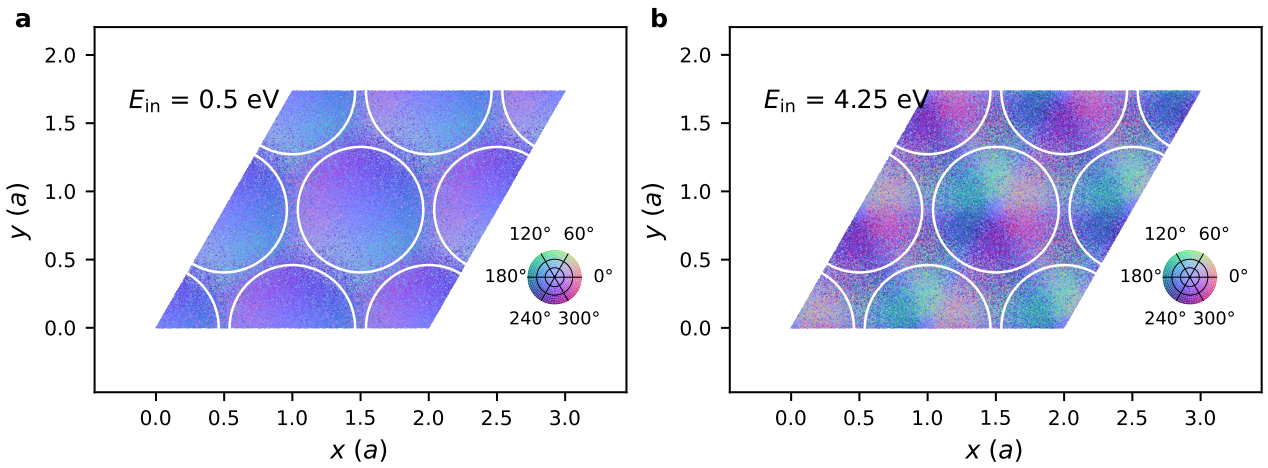

Figure S7: Hemispherical outgoing scattering angles depending on impact site in the surface unit cell of N_2 molecules in the vibrational ground states scattering from Ru(0001) with incidence energy of 0.5 eV (a) and 4.25 eV (a). Impact site coordinates are given as multiples of the surface lattice constant a. Color indicates scattering direction as depicted in the inset. Locations of surface atoms in the top layer are indicated by white circles. The unit cell is replicated into a 2×2 supercell for legibility only.

S3 Further Analysis of Rovibrational Energy Transfer

S3.1 Unrestricted Vibrational Energy Transfer

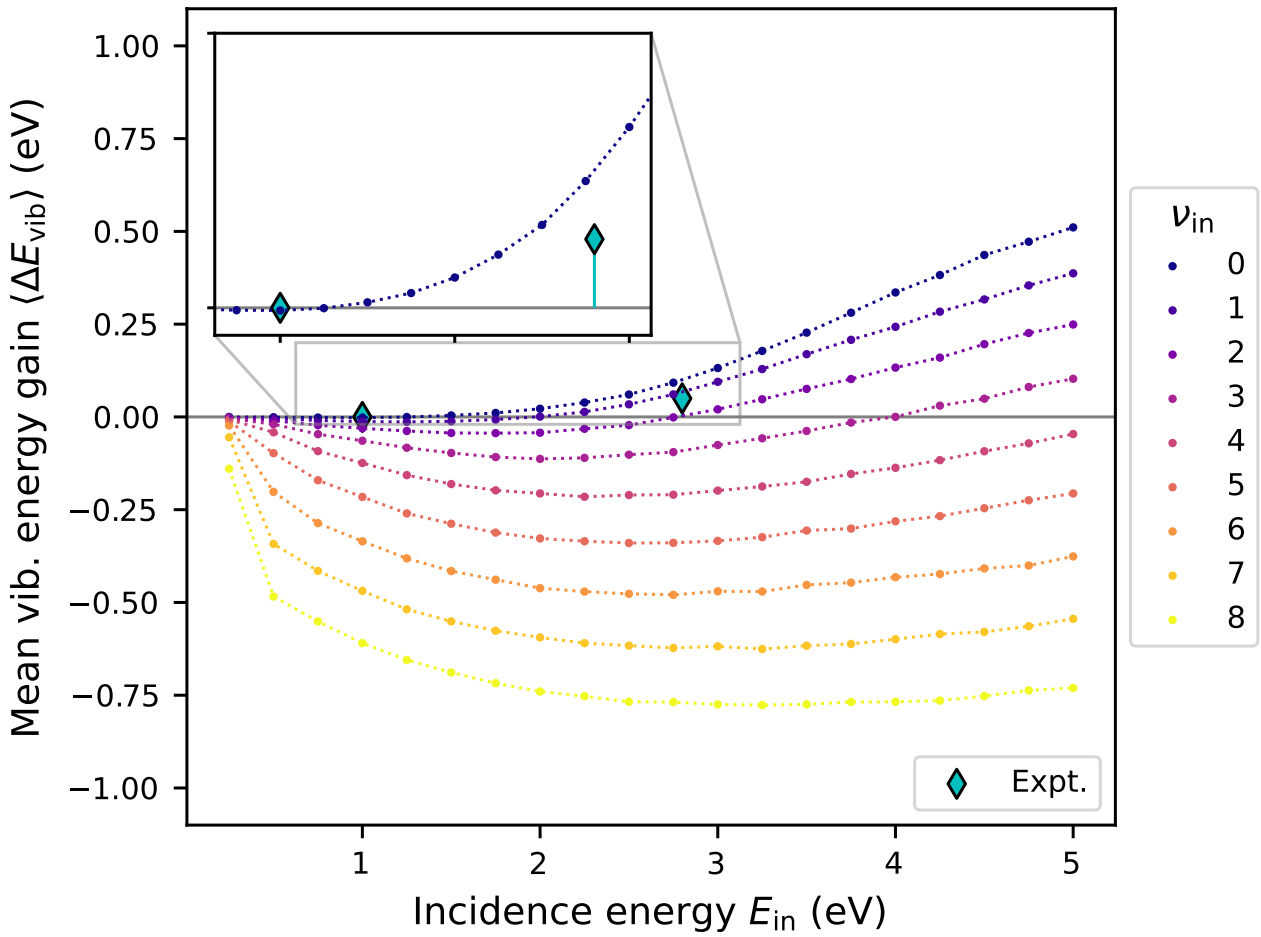

Figure S8: Mean vibrational energy gain $\langle \Delta E_{\text{vib}} \rangle$ over the incidence energy E_{in} per vibrational quantum ν_{in}. The cyan diamonds are experimental measurements by Mortensen et al. [4]. Other colors indicate the vibrational quantum number ν_{in}. The inset compares the vibrational ground state to the experiment. Same as Fig. 4, but without any restrictions for the rotational quantum numbers of the scattered N_2 molecules.

S3.2 Thermal Rotational Scattering

In this section, we motivate that the distribution of rotational energies of N_2 molecules after scattering from Ru(0001) can be well-approximated by a Boltzmann distribution, even though they differ significantly.

In Fig. S9, we show the probability density function and survival function of all scattered molecules from a monoenergetic beam with incidence energy 2.5 eV in the vibrational ground

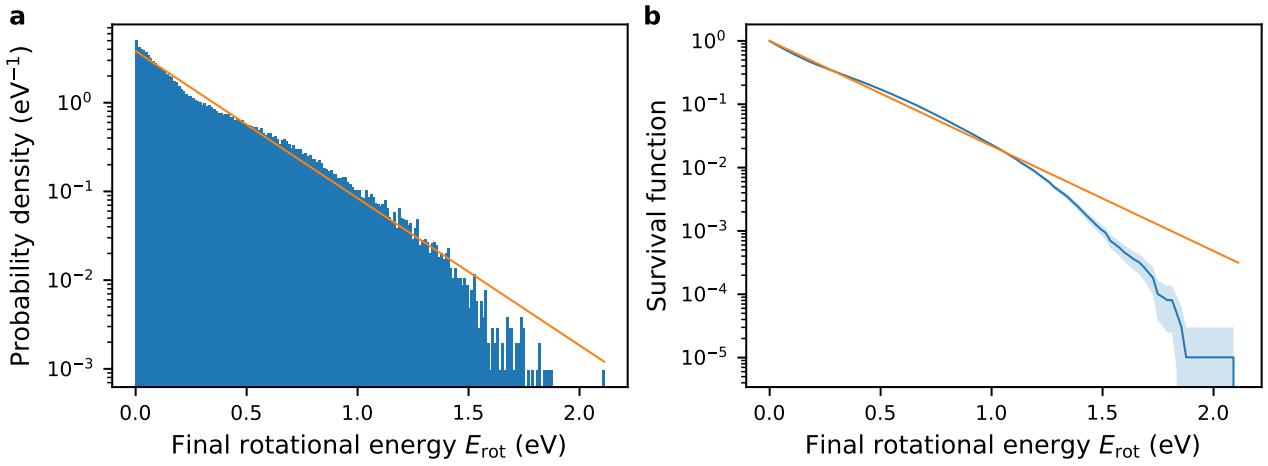

Figure S9: (a) Histogram of rotational energies of N_2 molecules in the vibrational ground state and incidence energy of 2.5 eV after scattering from Ru(0001). (b) Survival function according to the empirical cumulative distribution function of the same data with 95% confidence bounds. The orange lines are the probability density function and survival function of a Boltzmann distribution with the same mean energy.

state. Comparing the histogram and Boltzmann distributions in Fig. S9a, it is clear that these distributions are qualitatively very similar but quantitatively different. Comparing with the empirical survival function in Fig. S9b allows for a more quantitative statement as the Greenwood formula [5] can estimate the uncertainties of the empirical survival function. The Boltzmann distribution lies far outside of the confidence bounds in many regions, making the likelihood that they agree extremely unlikely. More rigorously, a Kolmogorov-Smirnov test [6] with significance level of $\alpha = 0.05$ rejects the hypothesis that the outgoing rotational energy is Boltzmann distribution for any $\nu \leq 8$ and $E_{in} = 0.25$–5.0 eV.

Statistically, we conclude that the rotational energy distribution is not Boltzmann distributed. Nevertheless, a Boltzmann distribution is still a good estimation in a physical sense: Its variance and skew match closely; The deviation of the cumulative distribution functions in terms of energy is only on the order of meV on average, with the only bad outliers at the tail of the distribution. These physical arguments outweigh the statistical arguments for the sake of analysis, all the while being aware of the approximation we make here.

S4 Vibrational State-to-State Scattering Distributions

As stated in the main article, we apply a histogram binning scheme to the classical action to determine the vibrational state-to-state scattering probabilities. In reality, this classical action is a continuous quantity in molecular dynamics and, thus, the state-to-state scattering probabilities are obtained by binning a continuous distribution of the outgoing classical action. Note that the incident action at $t = 0$ is quantized per the QCT method. In Fig. S10, we display the empirical cumulative distribution functions (CDFs) of the outgoing classical action from our QCT simulations. We also fit these CDFs with a mixture distribution of two distinct gamma distributions

$$\nu_{\mathrm{cl,out}} \sim p\,\mathrm{Gamma}(k_1, \theta_1) + (1 - p)\,\mathrm{Gamma}(k_2, \theta_2) \tag{S2}$$

using ordinary least squares. This is motivated by the bimodal nature of the distributions: one mode is usually centered around the incident quantum number resulting in nearly elastic scattering, while another broader mode represents the inelastic scattering event. The relative likelihood of these types of scattering is then given by p. This model fits very well to the data and may be used to determine the state-to-state scattering probabilities. In the limit cases for low and high incidence energy, we find that the forms of the distribution follows intuition: In the low energy limit $E_{\mathrm{in}}, E_{\mathrm{vib}} \to 0$, the scattering is nearly fully elastic and the distribution of the outgoing classical action is well-approximated by a sharp normal distribution. At the high incidence energy limit, where $E_{\mathrm{in}} \gg E_{\mathrm{vib}}$, we see that the distribution of the outgoing classical action is Boltzmann-like.

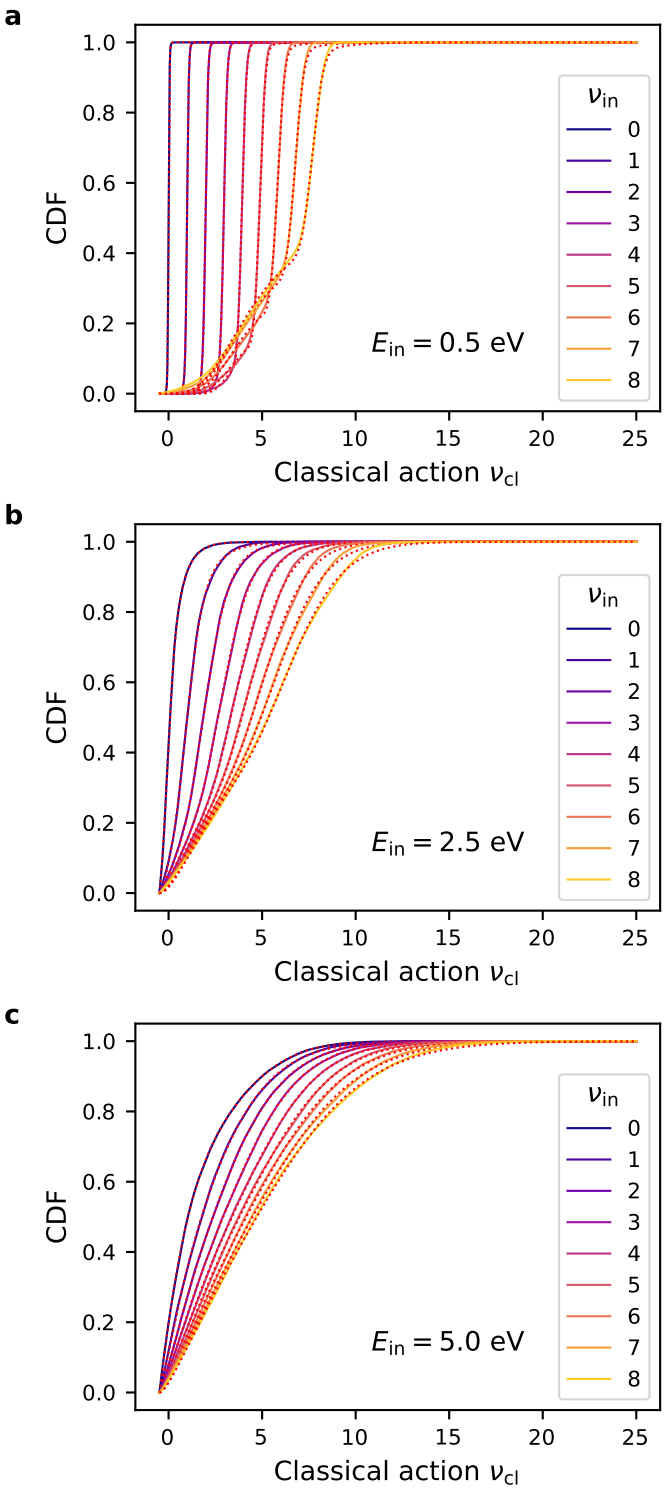

Figure S10: Empirical cumulative distribution functions of the vibrational classical action (as per Eq. (8)) without binning for incident vibrational quantum numbers $\nu_{in} \leq 8$ at incidence energies of 0.5 eV (a), 2.5 eV (b) and 5.0 eV (c). A mixture of two gamma distributions is fit to each cumulative distribution function (red dotted lines).

References

[1] Shakouri, K., Behler, J., Meyer, J., Kroes, G.-J.: Accurate neural network description of surface phonons in reactive gas–surface dynamics: N_2 + Ru(0001). J. Phys. Chem. Lett. **8**(10), 2131–2136 (2017) https://doi.org/10.1021/acs.jpclett.7b00784

[2] Huber, K.P., Herzberg, G.: Constants of diatomic molecules. In: Huber, K.P., Herzberg, G. (eds.) Molecular Spectra and Molecular Structure: IV. Constants of Diatomic Molecules, pp. 8–689. Springer, Boston, MA (1979). https://doi.org/10.1007/978-1-4757-0961-2_2

[3] Zaharia, T., Ueta, H., Kleyn, A.W., Gleeson, M.A.: Nitrogen Scattering at Ru(0001) Surfaces. Z. Für Phys. Chem. **227**(11), 1511–1522 (2013) https://doi.org/10.1524/zpch.2013.0415

[4] Mortensen, H., Jensen, E., Diekhöner, L., Baurichter, A., Luntz, A.C., Petrunin, V.V.: State resolved inelastic scattering of N_2 from Ru(0001). J. Chem. Phys. **118**(24), 11200–11209 (2003) https://doi.org/10.1063/1.1575210

[5] Greenwood, M.: A Report on the Natural Duration of Cancer. Reports on Public Health and Medical Subjects. H.M.S.O., London (1926)

[6] Kolmogorov, A.: Sulla determinazione empirica di una legge didistribuzione. G. Inst. Ital. Att. **4**, 89–91 (1933)